

3D Intra-cellular Wave Dynamics in a Phononic Plate with Ultra-wide Bandgap: Attenuation, Resonance and Mode Conversion

Saeid Hedayatrasa^{1*} and Mathias Kersemans^{1*}

¹ Mechanics of Materials and Structures (UGent-MMS), Department of Materials, Textiles and Chemical Engineering (MaTCh), Ghent University, Technologiepark-Zwijnaarde 46, 9052 Zwijnaarde, Belgium

Abstract

The intra-cellular wave dynamics of a water jetted phononic plate are experimentally investigated by means of high-resolution 3D scanning laser Doppler vibrometry. The study is focused on the vibrational behavior around the ultra-wide bandgap of the plate ([with a relative bandgap width of 0.89](#)), as the critical frequency range of its phononic functionality. Broadband vibrational excitations are applied using a piezoelectric transducer and both in-plane and out-of-plane operational deflection shapes of the unit-cells are analyzed with respect to mode shapes calculated by finite element simulation. Attenuation and resonance of both symmetric and antisymmetric wave modes are validated, and it is shown that despite the absence of in-plane wave energy actuation, the symmetric modes are effectively excited in the phononic lattice, due to mode conversion from co-existing antisymmetric modes. Supported by finite element modal analysis, this mode conversion observation is explained by the slight through-the-thickness asymmetry introduced during manufacturing of the phononic plate which leads to coupling of modes with different symmetry. The results confirm the potential of such detailed 3D inspection of phononic crystals (and in general acoustic metamaterials) in gaining full insight about their intracellular dynamics, which can also illuminate discrepancies with respect to idealized numerical models, that might be due to manufacturing imperfections.

Keywords: Phononic crystal, Bandgap, Guided waves, 3D Laser Doppler vibrometry, Intra-cellular dynamics, Mode conversion

1. Introduction

Phononic crystals are acoustic metamaterial lattices with extraordinary effects on elastic (and acoustic) wave propagation [1, 2]. A prominent characteristic of phononic crystals is the suppression of wave propagation over particular frequency ranges, so called phononic bandgaps. If a wave is incident to the phononic crystal at a bandgap frequency, its amplitude is exponentially attenuated through a few rows of phononic unit-cells. Moreover, a wave can be resonated and/or guided within the bandgap frequency range, through carefully designed features and canals introduced in the phononic lattice [3, 4]. Also when approaching the frequency regimes close to the bandgap edges, other promising characteristics e.g. flat wave front and negative

* Corresponding Authors:

saeid.hedayatrasa@ugent.be (S. Hedayatrasa), mathias.kersemans@ugent.be (M. Kersemans).

refraction index can be achieved [5], owing to the high anisotropic interaction of unit-cells with the incident wave. Consequently, carefully designing and combining phononic lattices enables filtration, steering, focusing and self-collimation of waves with applications in e.g. energy harvesting, fluid flow stabilization, [acoustic absorption](#), wireless communication and structural health monitoring [3, 6-15].

The underlying mechanism and the frequency range of a phononic bandgap substantially depend on the constitutive material(s), topology and the geometry of its unit-cell. In principle, a wave experiences high attenuation at a bandgap frequency due to its constructive reflection or its trapping and attenuation when interacting with the phononic unit-cells. The three well-known bandgap mechanisms are: (i) Bragg Scattering of waves at the interface of stiff scatterers embedded in a compliant matrix [3], (ii) Mie Resonance of waves in dense and compliant inclusions embedded in a stiff matrix [16], which can be further enhanced by adding (iii) Locally Resonant features to the unit-cell (e.g. a stiff and dense core inside a compliant shell) [17-19]. Hence, in order to activate a bandgap mechanism, it is essential to incorporate scattering or resonating features through a multi-material design and/or a cellular design with porosities [18, 20-23]. The bandgap efficiency of a phononic lattice can be further tuned through mechanical deformation or by incorporating active materials in the unit-cell design [24-26].

In order to maximize the phononic controllability of the unit-cell, it is necessary to achieve the widest phononic bandgap frequency range. Moreover, it is usually desired to minimize the bandgap frequency level so that the longest incident wavelength can be manipulated through a given unit-cell size [27]. For this purpose, the relative bandgap width (i.e. bandgap width divided by the mid-gap frequency) is maximized. Furthermore, the phononic lattice and its unit-cell can be designed so that particular wave types, e.g. bulk waves [28], surface waves [22], symmetric and/or antisymmetric guided waves modes, are exclusively controlled [29-31]. This has motivated many research works towards analysis, design and topology optimization of phononic crystals [19, 23, 25, 28, 32-40]. In earlier studies by current authors, phononic crystal plates were optimized for exclusive bandgaps of (i) symmetric or (ii) antisymmetric guided wave modes, and for (iii) complete bandgaps of mixed guided wave modes [29-31]. A cellular unit-cell design was considered which can be easily manufactured e.g. by perforation of a thin plate. Optimization of such cellular unit-cells for widest bandgaps is very challenging as it naturally converges towards tiny interconnecting features and, in fact, leads to impractical designs. Therefore, the current authors incorporated the effective stiffness of the phononic unit-cell in the topology optimization algorithm [29].

[The performance of phononic metamaterials may be experimentally evaluated by measuring the vibrational transmission spectrum to different unit-cells e.g. by means of piezoelectric transducers \(PZTs\) \[4, 30, 31, 41, 42\].](#) However, assessment of phononic crystals solely based on such transmission spectra from one point to another, is limited to the evaluation of bandgap

width and [its](#) transmission loss, and it does not provide any insights about the actual dynamic behavior of unit-cells and their activated vibrational modes. Other than the transmission loss inside the bandgap, achieving other aforementioned phononic functionalities is also of high importance, which are governed by the resonance modes of the unit-cell particularly in the vicinity of bandgap edges.

This has motivated the current study to investigate the guided wave's interaction with phononic plates, using a 3D infrared scanning laser Doppler vibrometer (SLDV) which gives access to both the out-of-plane and in-plane component of the wave field. Emergence of advanced SLDVs has enabled fast contact-free measurement of the vibrational response of components with complex geometry. The technique has been used in several preceding research works for validation of bandgap frequency ranges [38, 43-45], and full-field imaging and dispersion analysis of wave propagation [31, 46-49] in phononic metamaterials. [However, investigation of their 3D wave dynamics has been quite limited \[50-53\], and a study which can illuminate the full potential of the technique in inspection of both out-of-plane and in-plane modes, especially in the intra-cellular scale has not yet been reported.](#)

A topology with an ultra-wide complete bandgap of guided waves is selected from an earlier topology optimization study by the authors [31], which has been manufactured by water jetting a thin aluminum plate. Guided waves are excited using a PZT transducer bonded to the non-perforated border of the plate, and their interaction with the perforated phononic lattice is studied. The entire phononic plate is first scanned, followed by a high-resolution scanning focused on a mega unit-cell taken from the middle of the lattice. This allows to study the intra-cellular 3D wave dynamics. Symmetric and antisymmetric operational deflection shapes of the mega unit-cell are extracted and compared with calculated mode shapes of the unit-cell. It is shown that such detailed 3D inspection of the phononic lattice not only allows for validation of the attenuation of vibrations and resonance of phononic modes, but also reveals the coupling and conversion of modes stemming from the imperfection of water jetted cutting edges.

The paper is organized as follows. In section 2, the design and manufacturing of the phononic plate, the finite element (FE) analysis procedure and the experimental setup are explained. In section 3, the modes limiting the bandgap edges are studied in detail through FE simulation. In section 4, the experimental results of the phononic plate and the selected mega unit-cell are presented and discussed, followed by section 5, which supports the discrepancies observed in experiments through FE simulation of imperfect cutting edges. Conclusions are then summarized in section 6.

2. Material and Methodology

A phononic unit-cell with square symmetry and cellular topology as shown in [Figure 1\(a\)](#) is picked from the Pareto front of a multi-objective optimization study, which assures both widest bandgap at the lowest frequency level and maximized effective stiffness [31]. An aluminum plate with dimensions $400 \times 500 \text{ mm}^2$ is water jetted and a phononic lattice of 10 rows and 8 columns is manufactured ([Figure 1\(b-d\)](#)). The beam radius of the employed water jet has a value between 0.2-0.3 mm (it evolves over time due to erosion of the nozzle). The unit-cell has a designed width-to-thickness ratio of 10, and a resolution of 32×32 pixels. The plate has a nominal thickness of 2.5 mm (actual thickness is measured 2.42 mm), leading to a unit-cell width of $a = 25 \text{ mm}$, and a pixel size of 0.78 mm. As can be seen in [Figure 1\(d\)](#), the border of the plate is cut into 4 separate sections, each of which can be used for excitation of waves and studying its transmission to the other sections through the phononic lattice.

The modal band structure of the manufactured aluminum unit-cell is calculated through finite element analysis (FEA) using ANSYS APDL. The unit-cell is modeled with 92950 brick elements SOLID185 with linear formulation, reduced integration and hourglass control (20 layers through the thickness, and with an in-plane mesh size of 0.39 mm). Harmonic periodicity is applied through Floquet-Bloch boundary conditions by considering two superimposed meshes, and symmetric and antisymmetric modes are decoupled by applying relevant boundary conditions to the mid-thickness of plate [30]. An elastic modulus of 70 GPa, Poisson's ratio of 0.34 and density of 2700 kg/m^3 are assumed for simulation of the aluminum plate. [Figure 1\(e\)](#) shows the calculated modal band structure over the border of the irreducible Brillouin zone (the triangle ΓXM in the inset, in the periodic wave number space) which has been proven to be sufficient for modal band analysis of phononic crystals [27, 54].

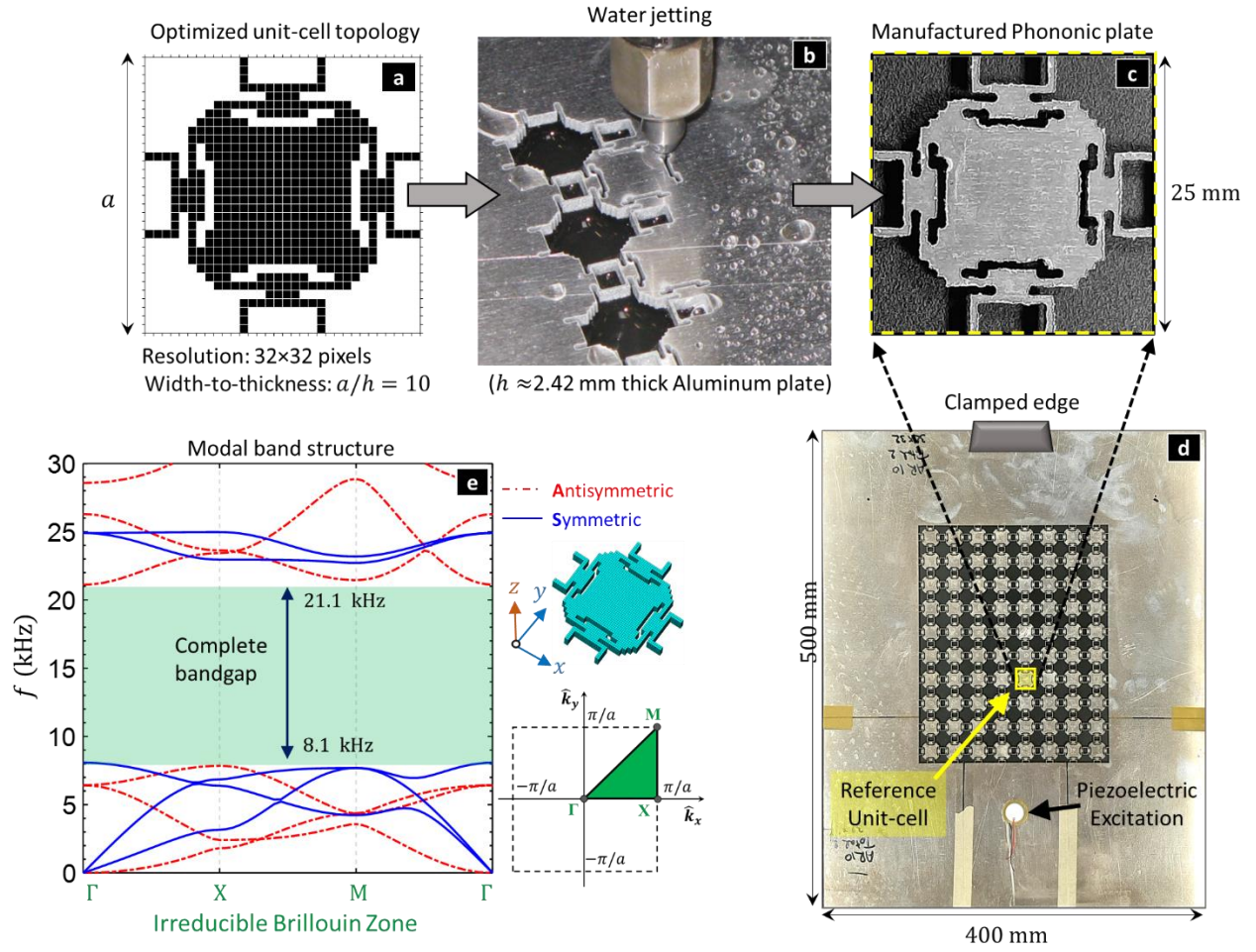


Figure 1. The phononic unit-cell with (a) an optimized cellular topology [31], manufactured by (b-d) water jetting an aluminum plate and (e) corresponding modal band structure calculated for a periodic unit-cell.

Different modal branches of guided waves are present, amongst which a complete bandgap of all modes is found in the frequency range 8.1 kHz to 21.1 kHz (Figure 1(e)). This leads to a relative bandgap width of 0.89, which is among the highest relative bandgap widths reported in the literature for a complete bandgap in such single material phononic plate [42, 47, 55].

In order to evaluate the vibrational response of the phononic plate, a PZT with a diameter of 27 mm (Elkuit EPZ-27MS44W) is glued to the lower side of the plate (Figure 1(d)) to excite waves, and the full-field velocity response is measured using a 3D SLDV (Polytec PSV-500-3D Xtra) with infrared measurement lasers. A linear frequency sweep between 1 Hz and 100 kHz, with a duration of 40 ms and amplitude of 50 V_{pp}, is supplied to the PZT using a waveform generator and a Falcon WMA-300 high-voltage amplifier. The vibrational response is measured at a sampling rate of 250 MS/s and with 10 averages for increased signal-to-noise ratio. The entire plate is first scanned with a spatial resolution of ~ 2 mm, followed by a detailed scan with spatial resolution of ~ 0.3 mm for visualization of the wave field within the unit-cells. Further, the

measurements are repeated for the same set-up but without any excitation, so that the corresponding measurement noise level is determined. The frequency response of the phononic plate is calculated using fast Fourier transform (FFT), and the transmission spectrums of both the out-of-plane velocity V_z and the in-plane velocity V_{xy} are studied. The plate is clamped at the middle of the upper edge during the measurement (see Figure 1 (d)).

3. Finite element modal analysis of the unit-cell

As the first step, the modal behavior of the unit-cell at frequencies limiting the bandgap are studied in detail through FEA. This provides more insight about the resonance modes expected at frequencies adjacent to the bandgap so that their actuation and existence in the experimental study can be confirmed. For this purpose, two modes D_1 and D_2 on the upper edge and three modes D_3 to D_5 on the lower edge of the bandgap are selected, as indicated on Figure 2.

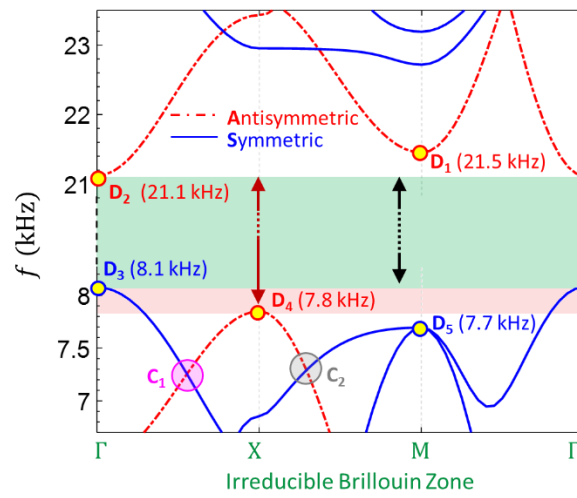


Figure 2. Modal band structure of the optimized phononic unit-cell around its bandgap, and indication of selected modes D_1 - D_5 on the bandgap edges.

A closer look at the bandgap edges in Figure 2 reveals that the exclusive bandgap of antisymmetric modes is further extended to a lower frequency of 7.8 kHz. Location of the selected modes in the irreducible Brillouin zone, corresponding wave vector and the relevant mode shapes are respectively shown in the left, middle and right columns of Figure 3.

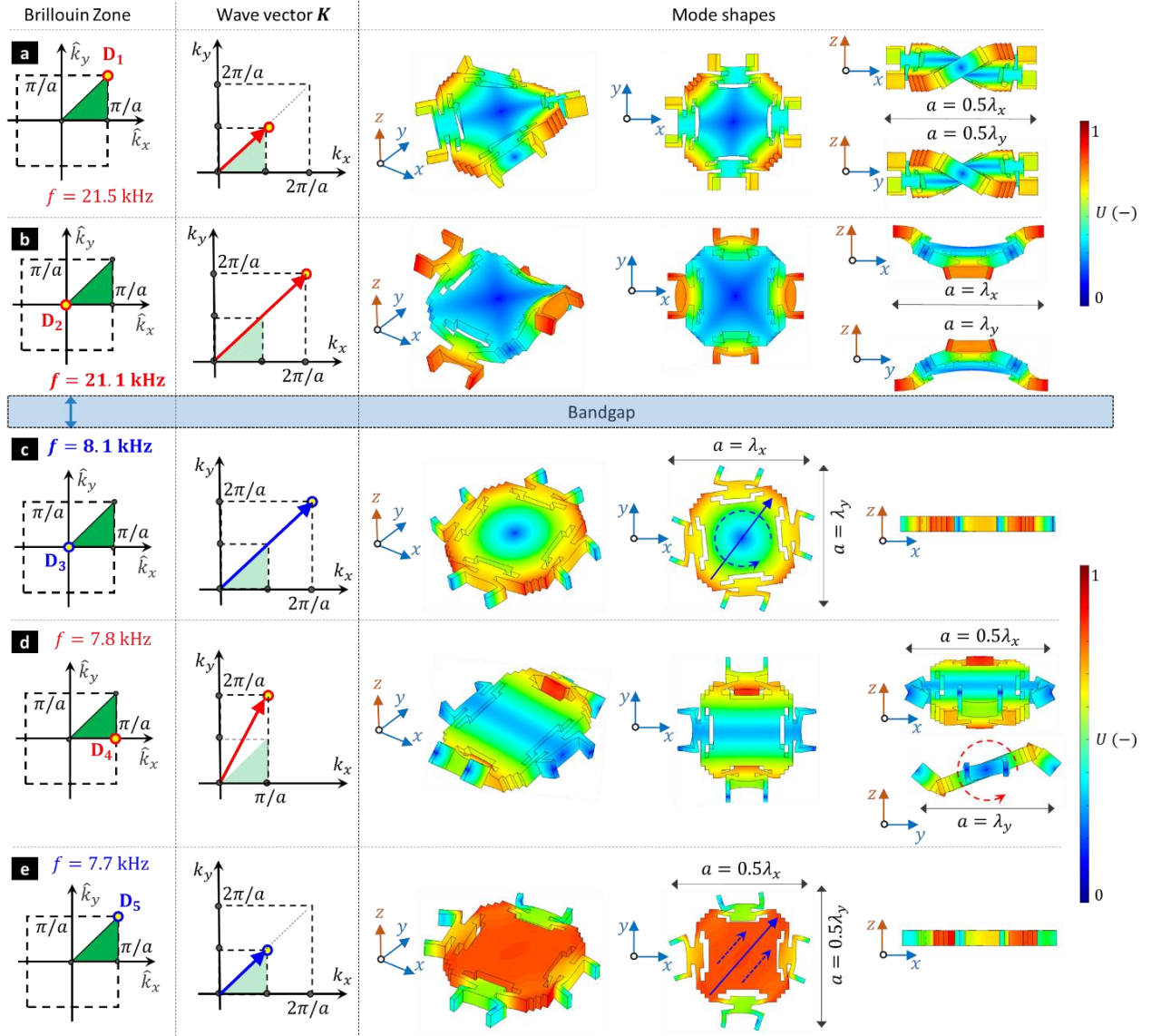


Figure 3. Modal analysis of the phononic unit-cell (a,b) at modes D_1 and D_2 on the upper edge of bandgap and (c-e) at modes D_3 to D_5 on the lower edge of bandgap. The color maps show the normalized value of total displacement U associated with the mode shapes.

The color maps show the normalized value of total displacement U . The wave vectors are added to indicate the wavelength and the direction of phase velocity corresponding to each mode. This is determined by analysis of the mode shapes of the unit-cell and the phase difference between its opposite faces to determine the wavelength $\lambda_x = 2\pi/k_x$ (and $\lambda_y = 2\pi/k_y$) in x-axis (and y-axis) with respect to the unit-cell size a . It can be seen that the wave vector $\mathbf{k} = \{k_x, k_y\}$ associated with each mode may be different from the reduced wave vector $\hat{\mathbf{k}} = \{\hat{k}_x, \hat{k}_y\}$. This is due to the harmonic periodicity of boundary conditions which folds back all modal branches to the first Brillouin zone.

According to Figure 3, the following can be understood:

- D_1 and D_2 are antisymmetric bending modes above the bandgap (Figure 3(a,b)), both with equal wavelengths in x- and y-axis leading to a wave vector along the diagonal axis of the unit-cell.
- D_3 is a symmetric mode with purely in-plane rotational deformation about z-axis shown by a dashed line arrow (Figure 3(c)). It has equal wavelengths in x- and y-axis, leading to a wave vector along the diagonal axis of the unit-cell shown by a solid line arrow.
- D_4 is an antisymmetric bending mode with a wavelength of two unit-cell sizes in x-axis and a wavelength of one unit-cell size in y-axis (Figure 3(d)). This leads to a wave vector inclined towards y-axis.
- D_5 is a symmetric mode with purely in-plane deformation (Figure 3(e)). It also has equal wavelengths in x- and y-axis leading to a wave vector along the diagonal axis of the unit-cell shown by a solid line arrow. The dashed line arrows show the longitudinal deformation of unit-cell parallel to the wave vector.

4. Measurement of the 3D wave dynamics

4.1. 3D SLDV of the phononic plate

In this section, the experimental results concerning full-field scanning of the phononic plate are presented and discussed. Figure 4(a) shows an arbitrary time snapshot of the wave field over the scanned area of the plate. Comparing the frequency spectrum of the excitation area 'E' with that of a reference unit-cell 'R' (on the 4th row of the lattice, also shown on Figure 1(d)) confirms the bandgap efficiency of the phononic plate for suppression of both out-of-plane component V_z (Figure 4(b)) and in-plane component V_{xy} (Figure 4(c)) of the excited wave field. The shaded area indicates the expected bandgap frequency range from the FEA (see Figure 2). Further, the measurement noise spectrum corresponding to the reference unit-cell demonstrates the performance of the bandgap for wave attenuation (Figure 1(d,e)). As can be seen, the noise level of the out-of-plane component V_z is lower than the noise level of in-plane component V_{xy} . This can be attributed to the specific angular configuration of the three laser heads of 3D SLDV, which in the current experimental setup favored the signal-to-noise ratio for the out-of-plane component.

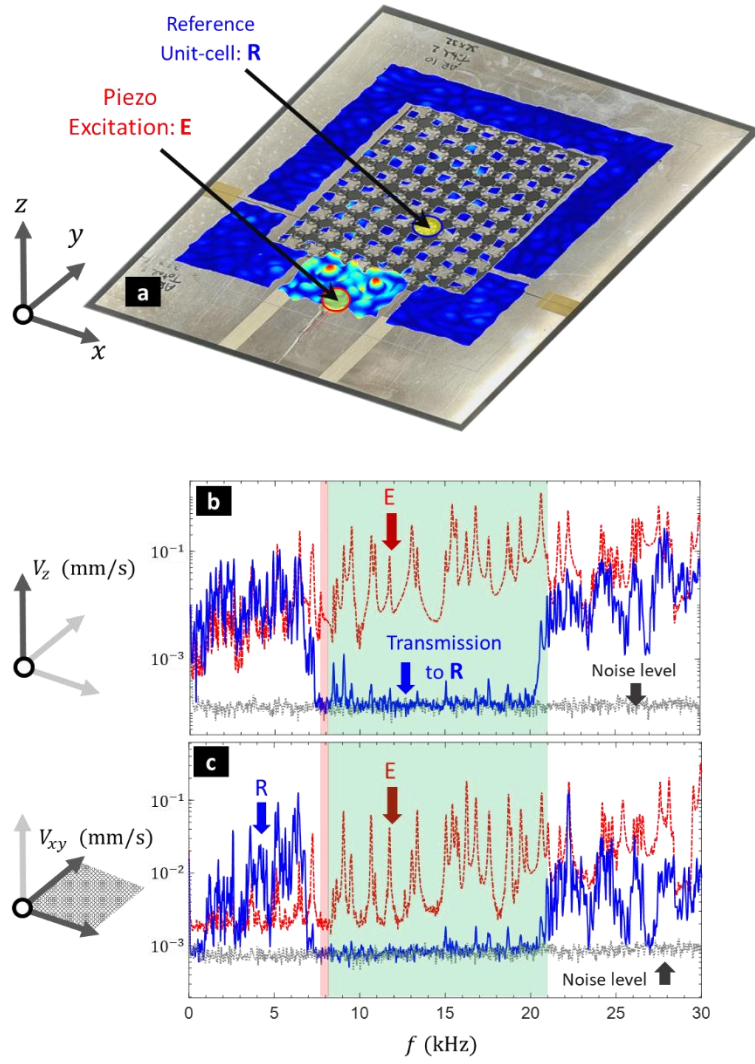


Figure 4. (a) 3D SLDV of the phononic plate. Frequency spectrum at the excitation area 'E' and at the reference unit-cell 'R': (b) out-of-plane velocity V_z and (c) in-plane velocity V_{xy} . The noise level is indicated by the gray dashed line. The shaded area indicates the bandgap frequency range obtained from the FEA (Figure 2). See appendix A for comparison of the measured transmission spectrum with FEA.

The spatial variation of bandgap is also confirmed in Figure 5 which shows the transmission spectrum along an entire column of unit-cells. The results clearly demonstrate that the wave's amplitude is significantly attenuated by each row of unit-cells and reaches the noise level after only 4 rows on which the reference unit-cell is located.

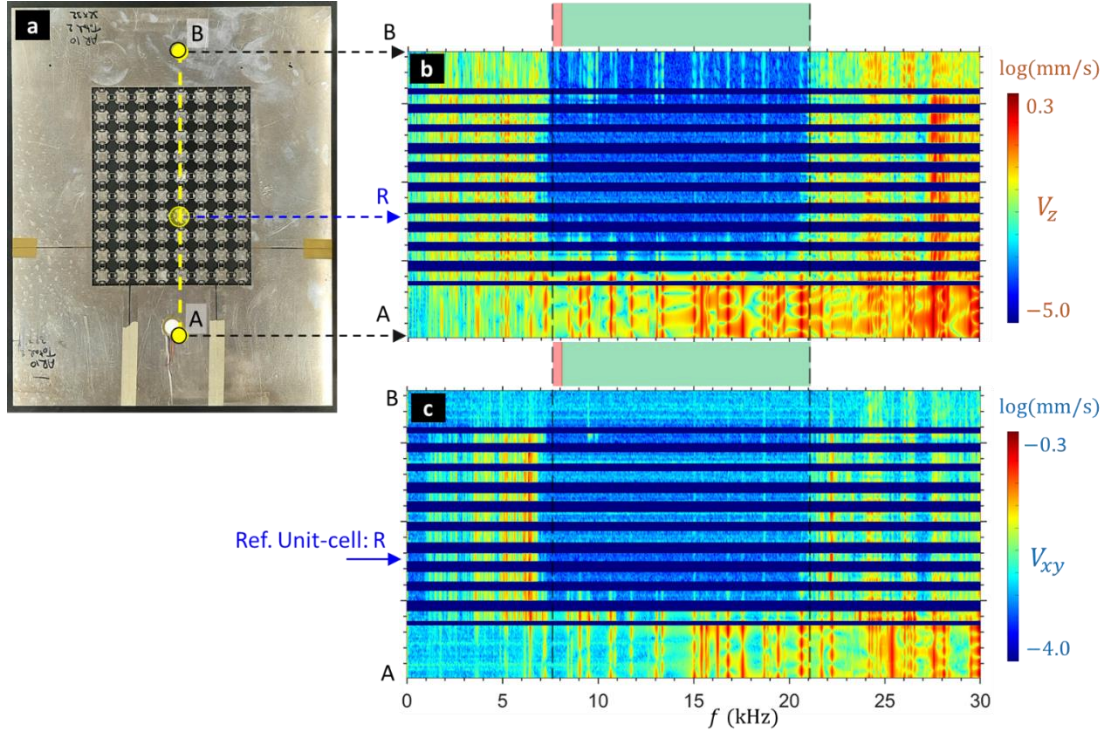


Figure 5. (a) Phononic plate. Frequency spectrum over the reference line AB along a single column of unit-cells: (b) out-of-plane velocity V_z and (c) in-plane velocity V_{xy} . The shaded area indicates the bandgap frequency range obtained from FEA (see Figure 2).

The experimentally measured bandgap range, which extends from 7 kHz up to 21 kHz (Figure 4 and Figure 5), also includes the additional range corresponding to the exclusive bandgap of antisymmetric modes (see the red shaded area in Figure 2). This is explained by the poor excitation of the symmetric modes of the plate at frequencies below the bandgap, as confirmed in Figure 4(c) and Figure 5(c). In fact, at such low frequencies, the symmetric modes have a relatively large wavelength (comparable to the global size of the plate), and may not be present in the finite size of the plate's border. For the same reason, the small PZT transducers have a weak coupling to the symmetric modes at low frequencies, and can only effectively excite the antisymmetric guided wave modes [56]. The reader is referred to appendix A in which the good correlation of experimental transmission spectrum with FEA results is confirmed.

It is expected that the lack of in-plane excitation leads to inefficient stimulation of the symmetric modes present on the lower edge of bandgap (Figure 1(e)). Nonetheless, the results show that the phononic lattice is quite significantly resonated at the frequencies below the bandgap and with a relatively high in-plane component (Figure 4(c) and Figure 5(c)).

This is further confirmed in Figure 6 which shows full-field frequency responses of the plate at three different frequencies 6.7, 15.0 and 21.0 kHz around the lower edge, the middle and the upper edge of the bandgap. The results demonstrate resonance and wave transmission

efficiency of the phononic lattice just outside the bandgap (Figure 6(a,b,e,f)), and its high attenuation inside the bandgap (Figure 6(c,d)), for both out-of-plane and in-plane components. At 6.7 kHz, the entire plate shows a relatively high out-of-plane response (Figure 6(a)), while the in-plane response is *only exclusively* present in the phononic lattice (Figure 6(b)). At this frequency, even the excitation side of plate shows almost no in-plane activation.

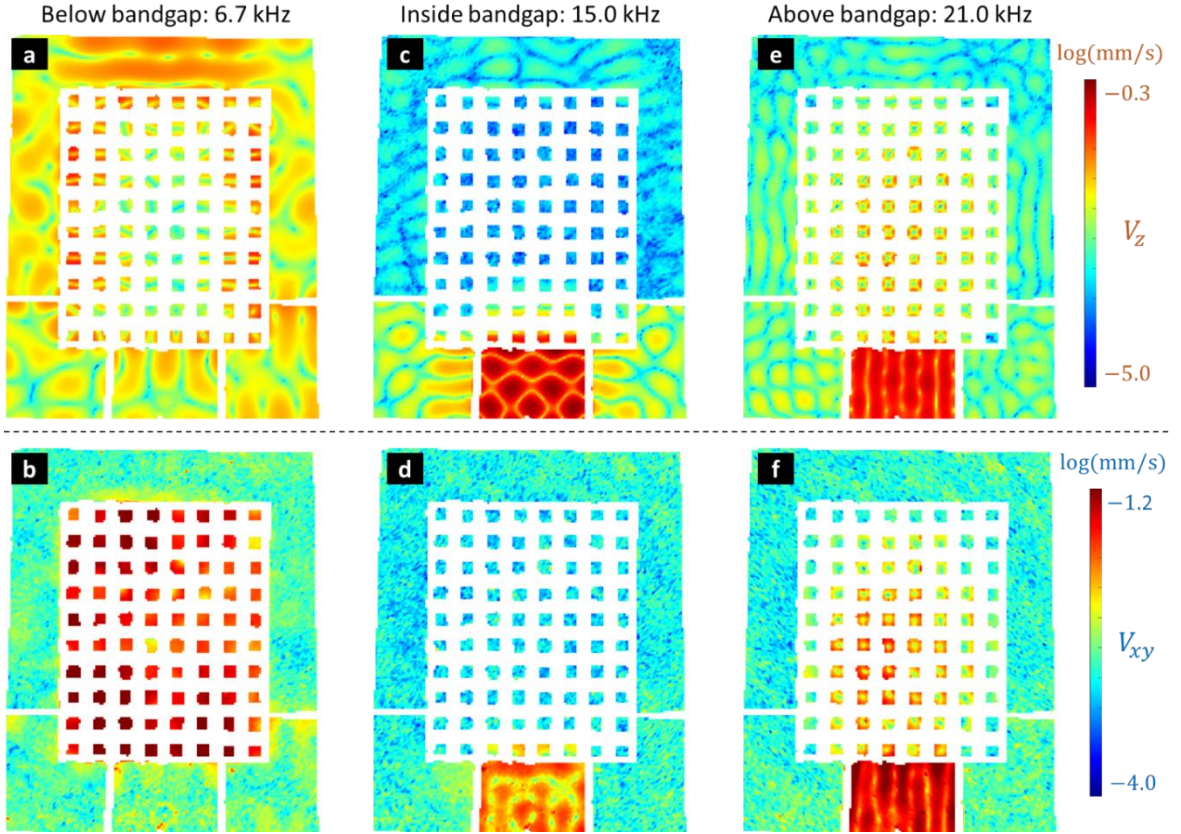


Figure 6. Full-field frequency response of the phononic plate at: (a,b) frequency 6.7 kHz, (c,d) frequency 15.0 kHz and (e,f) frequency 21.0 kHz. The top row shows the out-of-plane velocity V_z and the bottom row shows the in-plane velocity V_{xy} .

According to the modal band structure of the unit-cell below the bandgap (Figure 2, the area shaded in red), symmetric modes have to be present up to a higher frequency than antisymmetric modes. Nonetheless, the measured bandgap frequency range of both in-plane and out-of-plane responses is the same, and the presence of in-plane resonances is only observed when there is a co-existing antisymmetric mode (Figure 4-6). Hence, the distinctive in-plane response of the phononic lattice despite lack of in-plane excitation, can be explained by:

- the in-plane displacement associated with resonance of antisymmetric modes, and/or
- mode conversion from co-existing antisymmetric modes to symmetric modes, to be discussed later on, in section 5.

A high-resolution 3D SLDV scan of the phononic unit-cells can reveal which modes are present in the vibrational response, and can also explain the nature of the in-plane resonance observed at 6.7 kHz. This is the focus of the following section.

4.2. Intra-cellular high-resolution 3D SLDV

A high-resolution 3D SLDV measurement with a scanning grid of ~ 0.3 mm is performed over a mega unit-cell (i.e. the reference unit-cell and its four adjacent unit-cells), as shown in Figure 7.

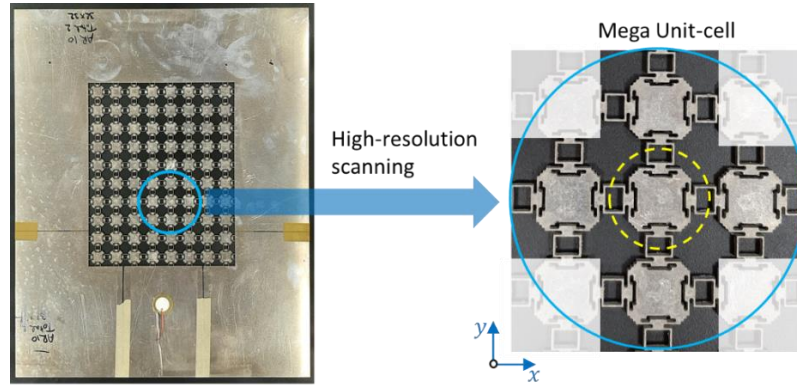


Figure 7. Close-up view of the mega unit-cell for which a high-resolution 3D SLDV measurement is performed

The out-of-plane and in-plane operational deflection shapes of the mega unit-cell are inspected at frequencies adjacent to the bandgap edges and are compared with the mode shapes expected from FE simulation (Figure 3). Different modes co-exist at bandgap edges which makes their individual identification from experimental results quite challenging. However, the frequencies that provide the most distinctive and almost exclusive indication of every individual mode shape are extracted and corresponding responses are shown in Figure 8. This includes frequencies 22.3 and 21.0 kHz just above the bandgap (Figure 8(a-d)), and frequencies 6.7, 6.5 and 6.4 kHz below the bandgap (Figure 8(e-j)). The left column shows the out-of-plane velocity V_z and the right column shows the in-plane velocity V_{xy} .

Carefully comparing the results with the mode shapes from FEA (Figure 3) confirms that all expected modes at the lower edge and upper edge of bandgap do exist in the response. This is understood based on the good match between the effective wavelengths in x- and y-axis and also the dominant polarization of the in-plane or out-of-plane components. The direction of the in-plane motion associated with symmetric modes is indicated by arrows in Figure 8(f,h,j). Animated operational deflection shapes are also provided in appendix B for better understanding of the 3D oscillations of the mega unit-cell at the selected frequencies, and are compared with animated mode shapes of a mega unit-cell from FEA of the phononic plate.

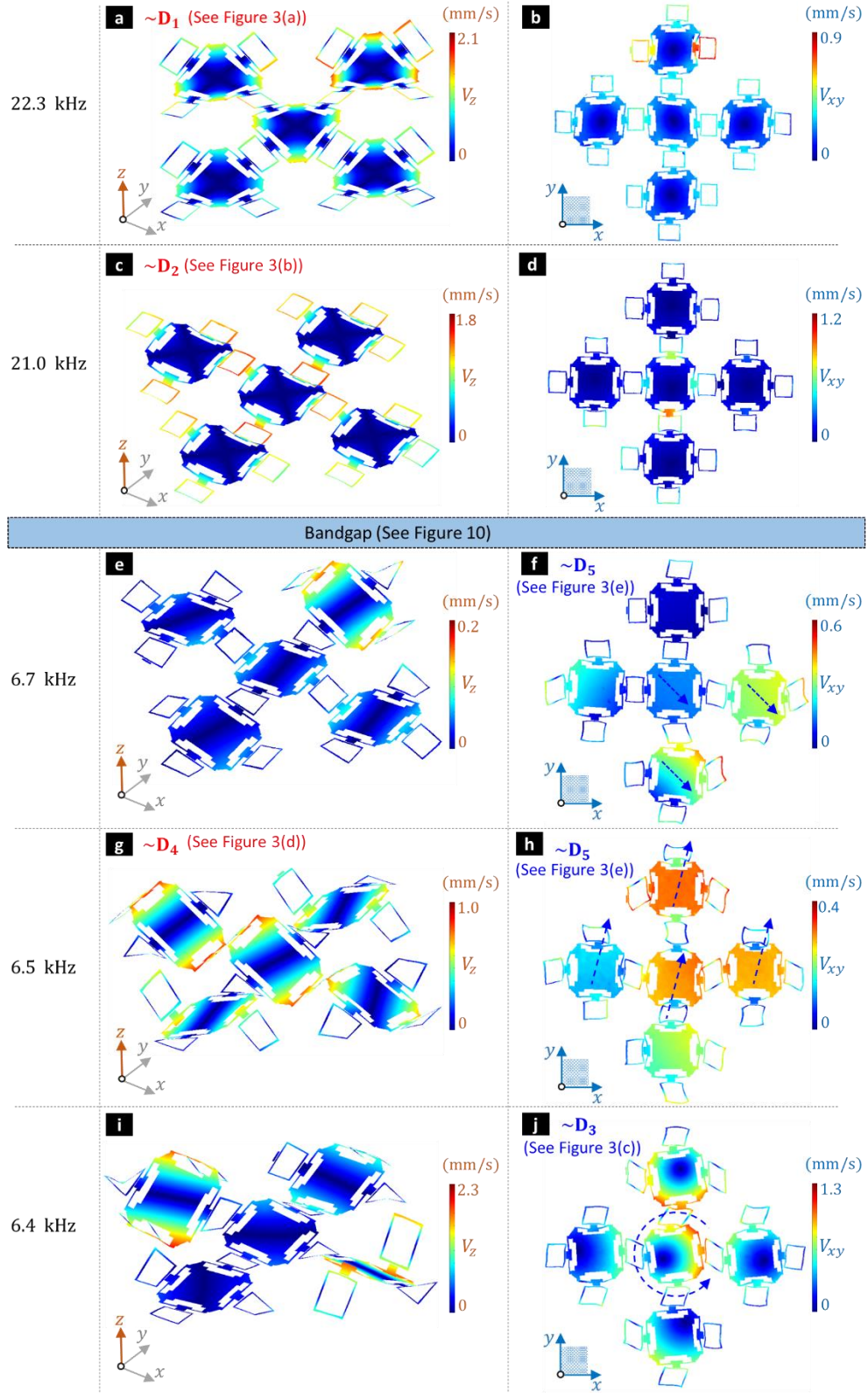


Figure 8. Measured operational deflection shapes of the mega unit-cell at selected frequencies (a-d) above bandgap and (e-j) below bandgap. The left column shows the out-of-plane velocity V_z and the right column shows the in-plane velocity V_{xy} . See appendix B for animated operational deflection shapes.

At frequencies above the bandgap, both antisymmetric modes D_1 and D_2 (Figure 3(a,b)) are present and distinctively excited at frequencies 21.0 kHz and 22.3 kHz (Figure 8(c,a)). There are no symmetric modes associated with the phononic unit-cell at these frequencies and the in-plane responses are induced by the antisymmetric resonances.

At frequencies below the bandgap, uncorrelated in-plane and out-of-plane responses are observed corresponding to co-existing symmetric and antisymmetric modes. The out-of-plane components (Figure 8(e,g,i)) show resonance of the antisymmetric mode, particularly at 6.5 kHz (Figure 8(g)) which resembles the mode shape of D_4 (Figure 3(e)). The in-plane component at 6.4 kHz (Figure 8(j)) indicates a pure symmetric mode equivalent to the mode D_3 (Figure 3(c)). Symmetric modes with dominantly longitudinal deformations are also observed at 6.5 and 6.7 kHz (Figure 8(h,f)) which are almost equivalent to the calculated mode D_5 (Figure 3(d)). There is also a minor indication of co-existing symmetric mode D_3 at these latter frequencies (see the animated operational deflection shapes in the supplementary materials).

The intra-cellular vibrational measurement also confirms the results of section 4.1 that despite very poor in-plane excitation of the plate, the symmetric modes are efficiently stimulated in the phononic region. This is even more significantly observed at 6.7 kHz showing a dominant in-plane vibrational response (Figure 8(e,f)). According to the operational deflection shapes of the mega unit-cell below the bandgap, this dominant in-plane response is due to resonance of symmetric modes, and not the in-plane component associated with antisymmetric modes. This can be explained by mode conversion from co-existing antisymmetric modes as explained later on, in the section 5.

Because of the very low vibrational response of the mega unit-cell within the bandgap, its response at a mid-gap frequency of 15 kHz is separately shown in Figure 9, in log scale. The results clearly show the high attenuation of both out-of-plane and in-plane components at this frequency.

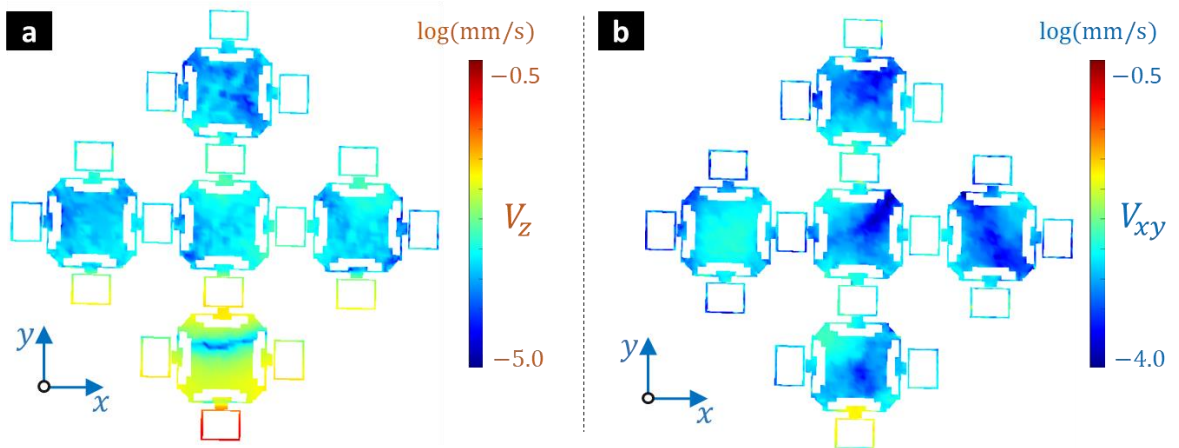


Figure 9. Vibrational response of the mega unit-cell at mid-gap frequency of 15 kHz: (a) out-of-plane velocity V_z and (b) in-plane velocity V_{xy} .

5. Asymmetry of water jetted edges and mode conversion

This section is dedicated to understanding the underlying reason of the mode conversion observed at the lower edge of bandgap in the 3D experimental results of section 4.

A detailed inspection of the manufactured phononic plate, reveals that the cutting edges are not perfectly square and there is a minor indication of non-uniform and asymmetric cutting edges (Figure 10(a,b)). As illustrated in Figure 10(c), this observation can be explained by an offset angle α in water jetting (e.g. due to an initial deflection or a small tilt of the plate while manufacturing) and also the well-known tapering effect in water jetting which leads to V-shaped or barrel-like edges [57, 58].

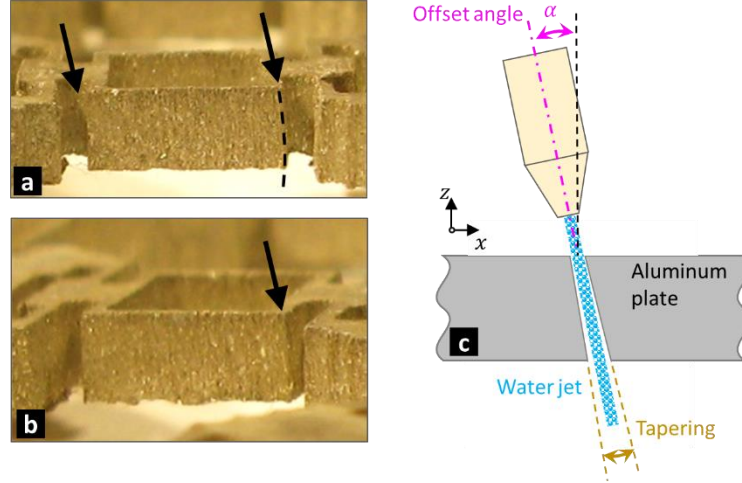


Figure 10. (a,b) Presence of asymmetric cutting edges in the phononic plate, due to (c) the tapering effect and/or an offset angle in water jetting

In a 2D phononic lattice with uniform through-the-thickness design, only modes of the same symmetry can couple and only in asymmetric planes of the lattice (e.g. over the edge XM of the irreducible Brillouin zone) [59]. However, any asymmetry of cutting edges can further lead to hybridization and coupling of different mode types, over the entire Brillouin zone. In order to understand the effect of such through-the-thickness asymmetry, the modal band structure is calculated for an obliquely perforated unit-cell with a small and constant offset angle of $\alpha = 2^\circ$. Although the modal band structure negligibly changes by such small offset angle, a close look at the intersection of modal branches reveals its substantial impact on the modal behavior of the unit-cell. As an example, a magnified view of the intersection C1 along the edge ΓX of the irreducible Brillouin zone (as indicated on Figure 2), is shown in Figure 11(a). From the results, it is clear that in case of perpendicular perforation (i.e. $\alpha = 0$), the two symmetric and antisymmetric modal branches are uncoupled and cross each other. However, after applying a small offset angle of $\alpha = 2^\circ$, the intersection disappears, the two modal branches split and a partial bandgap opens from around 7.15 kHz to around 7.25 kHz. The modes are hybrid, meaning that the purely symmetric and purely antisymmetric modes are not present anymore (see the insets of Figure 11(b)). In the upper modal branch, the hybrid (predominantly symmetric) mode

D3H1 converts to the hybrid (predominantly antisymmetric) mode D4H2. In the lower modal branch, the hybrid (predominantly antisymmetric) mode D4H1 converts to the hybrid (predominantly symmetric) mode D3H2. In fact, D3H1 and D3H2 are similar to the symmetric mode D3 (Figure 3(c)), but with minor out-of-plane displacement component. Likewise, D4H1 and D4H2 are similar to the antisymmetric mode D4 (Figure 3(d)), but with minor in-plane displacement component.

Figure 11(b) further demonstrates the variation of both the partial bandgap opened at intersection C_1 and the optimized complete bandgap of unit-cell, by variation of the offset angle α from 0 to 5°. The results show that the partial bandgap immediately opens by deviating the offset angle from $\alpha = 0^\circ$, and widens up to 0.21 kHz at $\alpha = 5^\circ$. The optimized bandgap with total width of 13 kHz at $\alpha = 0^\circ$ (from 8.1 kHz to 21.1 kHz, see Figure 2) slightly narrows down by 0.09 kHz at $\alpha = 5^\circ$.

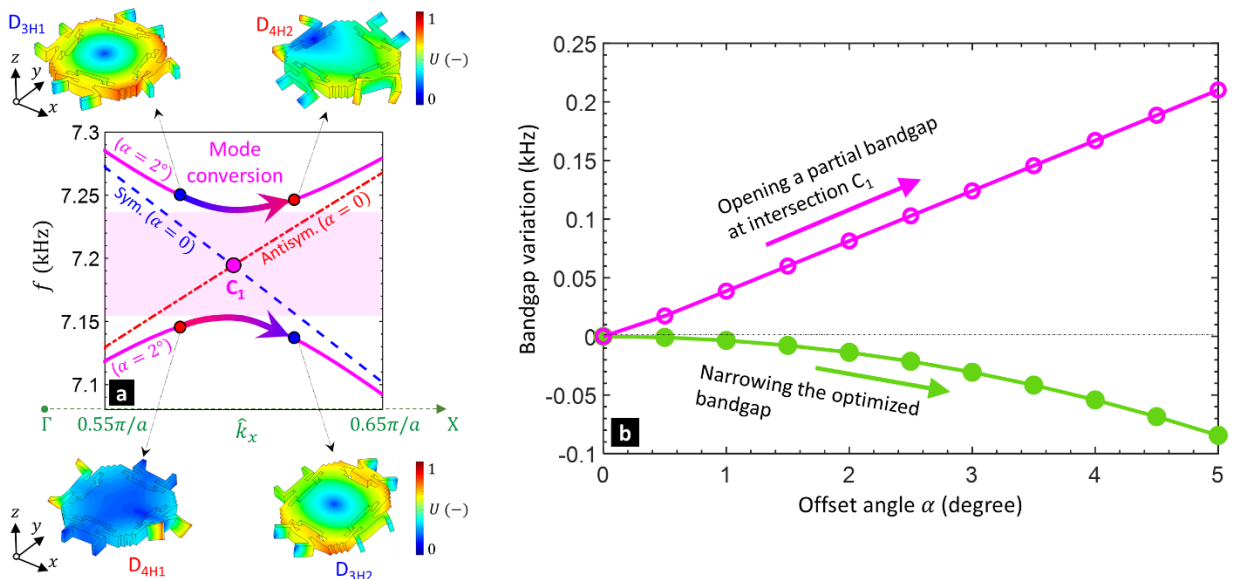


Figure 11. (a) Mode hybridization and mode conversion at the intersection C_1 between the modal branches D3 and D4 (see Figure 2) resulted from a small perforation offset angle of $\alpha = 2^\circ$ (with no tapering), and (b) opening a partial bandgap at intersection C_1 and narrowing the optimized bandgap in function of the offset angle α .

It can be shown that the same phenomenon occurs at other modal intersections, e.g. the intersection C_2 indicated on Figure 2. Therefore, even a small offset angle (or tapering) in water jetting of the phononic crystals can lead to coupling and mode conversion between symmetric and antisymmetric modes, while slightly changing the optimized bandgap width.

This can explain the mode conversion observed at the lower edge of the bandgap which, in the absence of in-plane incident wave energy, leads to resonance of symmetric modes within the phononic region. This can be clearly observed in the in-plane vibrational response of Figure 6(b), showing that the phononic lattice is adequately activated while the response of the plate's border

is in the noise level. In essence, at such low frequencies, the symmetric modes may not exist in the finite width of the plate's border and also may not couple to and get excited by the attached small PZT actuator. This is due to the relatively long wavelength of symmetric modes at the low frequencies below the bandgap, which is comparable to the global size of the tested plate.

6. Conclusions

A water jetted phononic plate with ultra-wide bandgap of guided waves is experimentally investigated, and its broadband frequency response is measured using 3D scanning laser Doppler vibrometry. Both out-of-plane and in-plane components of the guided wave field are analyzed. The attenuation and resonance behavior of the different wave modes is investigated, as well as mode coupling and mode conversion phenomena. The results confirm a promising bandgap efficiency for the plate in which both out-of-plane and in-plane components are attenuated to the measurement noise level. Furthermore, a high-resolution SLDV measurement is performed over a mega unit-cell chosen at the middle of the phononic lattice and its 3D operational deflection shapes are analyzed. Resonance of symmetric and antisymmetric modes at frequencies adjacent to the bandgap edges is confirmed and a good agreement with FEA of the phononic unit-cell is observed.

Due to the poor excitation of symmetric guided wave modes, the measured bandgap is effectively wider and rather corresponds to the exclusive bandgap of antisymmetric modes. Nonetheless, it is shown that the symmetric modes of the phononic unit-cells are effectively stimulated due to mode conversion from the co-existing antisymmetric modes. With the support of finite element modal analysis, this observation is explained by the hybridization and coupling of symmetric and antisymmetric modes due to a slight asymmetry of water jetted cutting edges. This observation, demonstrates the great potential of such detailed 3D inspection in revealing manufacturing-induced deviations of the unit-cell's dynamic response from simulation, which may not be achieved through a simple measurement of transmission spectrum between two points. Moreover, it explains why the symmetric modes of the phononic plate get excited when interacting with a predominantly out-of-plane incident wave (which is more easily excited in practice). Therefore, one may consider such asymmetric cutting in the design stage of phononic lattice, at locations where energy transfer and coupling between dissimilar mode types is desired.

Appendix A. Transmission spectrum to the reference unit-cell (SLDV versus FEA)

In this appendix, the transmission spectrum of guided waves from the PZT excitation to the reference unit-cell is calculated through FEA and is compared with SLDV measurements. The transmission spectrum is calculated as the ratio of average (i.e. root mean square) response over the entire unit-cell divided by the average response over the excitation area.

The entire phononic plate is simulated by ABAQUS CAE, with an in-plane mesh resolution of 0.39 mm and using one layer of continuum shell elements SC8R with linear formulation, reduced integration and hourglass control. The PZT transducer is modeled using brick piezoelectric elements C3D8E, and NCE51 piezoceramic material properties provided by the manufacturer (NOLIA[®] Kvistgård, Denmark) are used. Steady state harmonic response of the phononic plate is calculated up to 30 kHz and with a frequency resolution of 50 Hz.

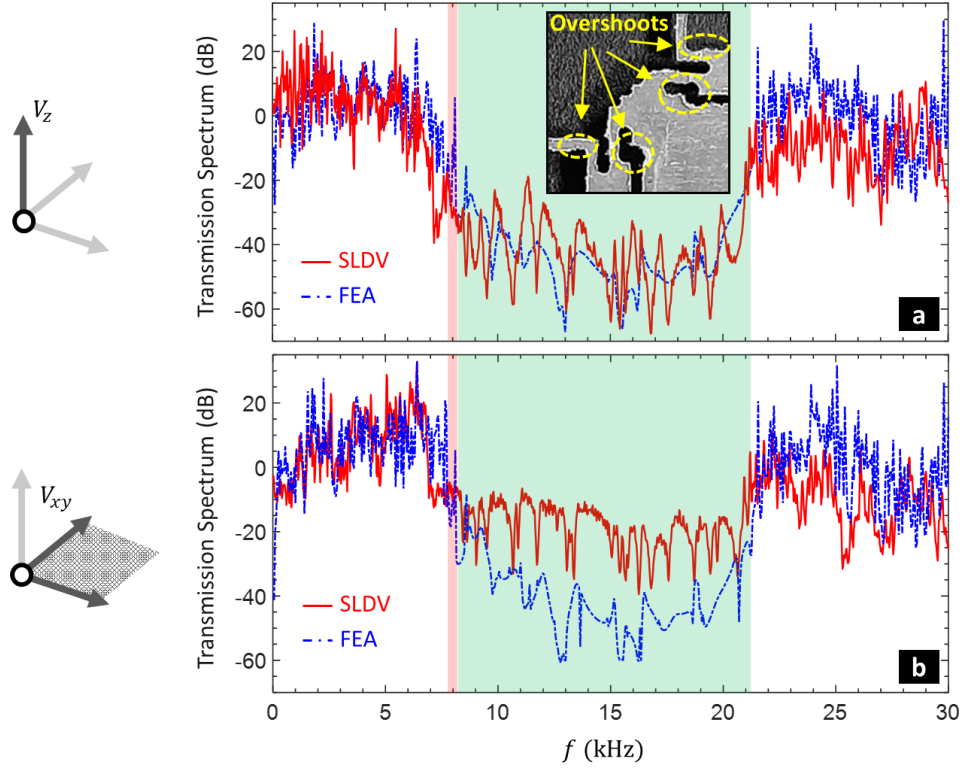


Figure A1. Transmission spectrum of guided waves from PZT transducer to the reference unit-cell, from both SLDV measurement and steady state harmonic FEA: (a) out-of-plane response and (b) in-plane response

By comparison of the experimental and FEA transmission spectra, a good agreement in the bandgap frequency range of both the out-of-plane and in-plane responses is observed (Figure A1). However, one may realize that the experimental transmission loss starts at a slightly lower frequency than the simulation. This minor discrepancy can be explained by the overshooting visible in the water jetted unit-cells (see an example in the inset of Figure A1(a)) which reduces the effective stiffness of the unit-cell and leads to a small deviation of effective bandgap properties. As expected, the experimental transmission loss inside the bandgap is lower than FEA due to the presence of measurement noise, particularly for the in-plane response which has a higher noise level in the current experimental set-up.

Appendix B. Animated response of the mega unit-cell (SLDV versus FEA)

(To be possibly made available online by the journal as an appendix with a direct link to animations. Otherwise, provided as supplementary materials.)

The same finite element model developed in appendix A is further solved for modal analysis of the phononic plate. Mode shapes of the mega unit-cell are extracted and compared with the measured operational deflection shapes.

References

1. Deymier, P., *Acoustic metamaterials and phononic crystals*. 2011: Springer.
2. Li, W., et al., *Topology optimization of photonic and phononic crystals and metamaterials: a review*. Advanced Theory and Simulations, 2019. **2**(7): p. 1900017.
3. Olsson Iii, R.H. and I.F. El-Kady, *Microfabricated phononic crystal devices and applications*. Measurement Science and Technology, 2009. **20**(1): p. 012002.
4. Krushynska, A.O., et al., *Arbitrary-curved waveguiding and broadband attenuation in additively manufactured lattice phononic media*. Materials & Design, 2021. **205**: p. 109714.
5. Astolfi, L., et al. *Negative refraction in conventional and additively manufactured phononic crystals*. in 2019 IEEE International Ultrasonics Symposium (IUS). 2019. IEEE.
6. El-Kady, I., R. Olsson, and J. Fleming, *Phononic band-gap crystals for radio frequency communications*. Applied Physics Letters, 2008. **92**(23): p. 233504-233504-3.
7. Lv, H., et al., *Vibration energy harvesting using a phononic crystal with point defect states*. APPLIED PHYSICS LETTERS, 2013. **102**: p. 034103.
8. Semperlotti, F. and H. Zhu, *Achieving selective interrogation and sub-wavelength resolution in thin plates with embedded metamaterial acoustic lenses*. Journal of Applied Physics, 2014. **116**(5): p. 054906.
9. Hussein, M., et al., *Flow stabilization by subsurface phonons*, in *Proceedings of the Royal Society of London A: Mathematical, Physical and Engineering Sciences*. 2015, The Royal Society. p. 20140928.
10. Ciampa, F., A. Mankar, and A. Marini, *Phononic Crystal Waveguide Transducers for Nonlinear Elastic Wave Sensing*. Scientific Reports, 2017. **7**(1): p. 14712.
11. Miniaci, M., et al., *Proof of concept for an ultrasensitive technique to detect and localize sources of elastic nonlinearity using phononic crystals*. Physical review letters, 2017. **118**(21): p. 214301.
12. Gao, N. and K. Lu, *An underwater metamaterial for broadband acoustic absorption at low frequency*. Applied Acoustics, 2020. **169**: p. 107500.
13. Shan, S., F. Wen, and L. Cheng, *Purified nonlinear guided waves through a metamaterial filter for inspection of material microstructural changes*. Smart Materials and Structures, 2021. **30**(9): p. 095017.
14. Liao, G., et al., *Broadband controllable acoustic focusing and asymmetric focusing by acoustic metamaterials*. Smart Materials and Structures, 2021. **30**(4): p. 045021.
15. Hu, G., et al., *Acoustic-Elastic Metamaterials and Phononic Crystals for Energy Harvesting: A Review*. Smart Materials and Structures, 2021.
16. Brunet, T., J. Leng, and O. Mondain-Monval, *Soft acoustic metamaterials*. Science, 2013. **342**(6156): p. 323-324.
17. Liu, Z., et al., *Locally resonant sonic materials*. Science, 2000. **289**(5485): p. 1734-1736.

18. Mizukami, K., et al., *Three-dimensional printing of locally resonant carbon-fiber composite metastructures for attenuation of broadband vibration*. Composite Structures, 2021. **255**: p. 112949.
19. Hedayatrasa, S., K. Abhary, and M. Uddin. *On topology optimization of acoustic metamaterial lattices for locally resonant bandgaps of flexural waves*. in *Proceedings of ACOUSTICS 2016: The Second Australasian Acoustical Societies Conference*. 9-11 November 2016, Brisbane, Australia.
20. Mehaney, A. and A.M. Ahmed, *Locally Resonant Phononic Crystals at Low frequencies Based on Porous SiC Multilayer*. Scientific Reports, 2019. **9**(1): p. 14767.
21. Yuan, L., et al., *Study on Lamb Waves in a Composite Phononic Crystal Plate*. Crystals, 2020. **10**(9): p. 799.
22. Liu, Z., H.-W. Dong, and G.-L. Yu, *Topology optimization of periodic barriers for surface waves*. Structural and Multidisciplinary Optimization, 2021. **63**(1): p. 463-478.
23. Hedayatrasa, S., et al., *Introducing obliquely perforated phononic plates for enhanced bandgap efficiency*. Materials, 2018. **11**(8): p. 1309.
24. Wang, Y.-F., et al., *Tunable and Active Phononic Crystals and Metamaterials*. Applied Mechanics Reviews, 2020. **72**(4).
25. Hedayatrasa, S., et al., *Optimal design of tunable phononic bandgap plates under equibiaxial stretch*. Smart Materials and Structures, 2016. **25**(5): p. 055025.
26. Hedayati, R. and S. Lakshmanan, *Pneumatically-Actuated Acoustic Metamaterials Based on Helmholtz Resonators*. Materials, 2020. **13**(6): p. 1456.
27. Sigmund, O., *Systematic Design of Metamaterials by Topology Optimization*, in *IUTAM Symposium on Modelling Nanomaterials and Nanosystems*, R. Pyrz and J.C. Rauhe, Editors. 2009, Springer Netherlands. p. 151-159.
28. Lu, Y., et al., *3-D phononic crystals with ultra-wide band gaps*. Scientific Reports, 2017. **7**(1): p. 43407.
29. Hedayatrasa, S., et al., *Optimum design of phononic crystal perforated plate structures for widest bandgap of fundamental guided wave modes and maximized in-plane stiffness*. Journal of the Mechanics and Physics of Solids, 2016. **89**: p. 31-58.
30. Hedayatrasa, S., et al., *Maximizing bandgap width and in-plane stiffness of porous phononic plates for tailoring flexural guided waves: Topology optimization and experimental validation*. Mechanics of Materials, 2017. **105**: p. 188-203.
31. Hedayatrasa, S., et al., *Optimization and experimental validation of stiff porous phononic plates for widest complete bandgap of mixed fundamental guided wave modes*. Mechanical Systems and Signal Processing, 2018. **98**: p. 786-801.
32. D'Alessandro, L., et al., *Shape optimization of solid-air porous phononic crystal slabs with widest full 3D bandgap for in-plane acoustic waves*. Journal of Computational Physics, 2017. **344**: p. 465-484.
33. Bortot, E., O. Amir, and G. Shmuel, *Topology optimization of dielectric elastomers for wide tunable band gaps*. International Journal of Solids and Structures, 2018. **143**: p. 262-273.
34. Chen, J., B. Xia, and J. Liu, *A sparse polynomial surrogate model for phononic crystals with uncertain parameters*. Computer Methods in Applied Mechanics and Engineering, 2018. **339**: p. 681-703.
35. Boukadia, R.F., et al., *A wave-based optimization framework for 1D and 2D periodic structures*. Mechanical Systems and Signal Processing, 2020. **139**: p. 106603.
36. Liang, X. and J. Du, *Design of phononic-like structures and band gap tuning by concurrent two-scale topology optimization*. Structural and Multidisciplinary Optimization, 2020. **61**(3): p. 943-962.
37. Bilal, O.R. and M.I. Hussein, *Ultrawide phononic band gap for combined in-plane and out-of-plane waves*. Physical Review E, 2011. **84**(6): p. 065701.

38. Bilal, O.R., A. Foehr, and C. Daraio, *Enhancement of deep-subwavelength band gaps in flat spiral-based phononic metamaterials using the trampoline phenomena*. Journal of Applied Mechanics, 2020. **87**(7).
39. Palermo, A. and A. Marzani, *A reduced Bloch operator finite element method for fast calculation of elastic complex band structures*. International Journal of Solids and Structures, 2020. **191-192**: p. 601-613.
40. Zega, V., et al., *Experimental proof of emergent subharmonic attenuation zones in a nonlinear locally resonant metamaterial*. Scientific reports, 2020. **10**(1): p. 1-11.
41. Miranda Jr, E.J.P., et al., *Wave attenuation in elastic metamaterial thick plates: Analytical, numerical and experimental investigations*. International Journal of Solids and Structures, 2020. **204-205**: p. 138-152.
42. D'Alessandro, L., et al., *Modeling and experimental verification of an ultra-wide bandgap in 3D phononic crystal*. Applied Physics Letters, 2016. **109**(22): p. 221907.
43. Zouari, S., J. Brocaill, and J.M. G  nevaux, *Flexural wave band gaps in metamaterial plates: A numerical and experimental study from infinite to finite models*. Journal of Sound and Vibration, 2018. **435**: p. 246-263.
44. Meng, H., et al., *3D rainbow phononic crystals for extended vibration attenuation bands*. Scientific Reports, 2020. **10**(1): p. 18989.
45. Gao, N., et al., *Elastic wave modulation of double-leaf ABH beam embedded mass oscillator*. Applied Acoustics, 2021. **173**: p. 107694.
46. Zhou, C., et al., *Numerical and experimental investigation on broadband wave propagation features in perforated plates*. Mechanical Systems and Signal Processing, 2016. **75**: p. 556-575.
47. Miniaci, M., et al., *Experimental Observation of a Large Low-Frequency Band Gap in a Polymer Waveguide*. Frontiers in Materials, 2018. **5**(8).
48. Wang, T.-T., et al., *Collective resonances of a chain of coupled phononic microresonators*. Physical Review Applied, 2020. **13**(1): p. 014022.
49. Kherraz, N., et al., *Experimental full wavefield reconstruction and band diagram analysis in a single-phase phononic plate with internal resonators*. Journal of Sound and Vibration, 2021. **503**: p. 116098.
50. Celli, P. and S. Gonella, *Laser-enabled experimental wavefield reconstruction in two-dimensional phononic crystals*. Journal of Sound and Vibration, 2014. **333**(1): p. 114-123.
51. Celli, P. and S. Gonella, *Manipulating waves with LEGO® bricks: A versatile experimental platform for metamaterial architectures*. Applied Physics Letters, 2015. **107**(8): p. 081901.
52. Andreassen, E., K. Manktelow, and M. Ruzzene, *Directional bending wave propagation in periodically perforated plates*. Journal of Sound and Vibration, 2015. **335**: p. 187-203.
53. Miniaci, M., et al., *Experimental observation of topologically protected helical edge modes in patterned elastic plates*. Physical Review X, 2018. **8**(3): p. 031074.
54. Maurin, F., et al., *Probability that a band-gap extremum is located on the irreducible Brillouin-zone contour for the 17 different plane crystallographic lattices*. International Journal of Solids and Structures, 2018. **135**: p. 26-36.
55. Jiang, S., H. Hu, and V. Laude, *Ultra - Wide Band Gap in Two - Dimensional Phononic Crystal with Combined Convex and Concave Holes*. physica status solidi (RRL) – Rapid Research Letters, 2018. **12**(2): p. 1700317.
56. Giurgiutiu, V. *Lamb wave generation with piezoelectric wafer active sensors for structural health monitoring*. in *Smart Structures and Materials 2003: Smart Structures and Integrated Systems*. 2003. International Society for Optics and Photonics.
57. Wang, S., et al., *Exploring cutting front profile in abrasive water jet machining of aluminum alloys*. The International Journal of Advanced Manufacturing Technology, 2021. **112**(3): p. 845-851.

58. Bañon, F., et al., *A Review on the Abrasive Water-Jet Machining of Metal–Carbon Fiber Hybrid Materials*. Metals, 2021. **11**(1): p. 164.
59. Chen, J.-J., B. Bonello, and Z.-L. Hou, *Plate-mode waves in phononic crystal thin slabs: mode conversion*. Physical Review E, 2008. **78**(3): p. 036609.